Research Paper

A case study of ozone diurnal variation in the convective boundary layer in the southeastern United States using multiple observations and large eddy simulation

Guanyu Huang[1*], M.J. Newchurch[2], Shi Kuang[3], Huug G. Ouwersloot[3]

1. Environmental and Health Program, Spelman College, Atlanta GA USA, 30314
2. Atmospheric Science Department, the University of Alabama in Huntsville, Huntsville AL, U.S. 35805.
3. Earth System Science Center, University of Alabama in Huntsville, Huntsville, AL, U.S. 35805.
4. Max Planck Institute for Chemistry, Mainz, Germany, D55122

*corresponding author: Guanyu Huang, Environmental and Health Program, Spelman College, Atlanta, GA, 30314; ghuang@spelman.edu

Abstract

We investigate the ozone diurnal variation on September 6, 2013 under a midsize urban environment using multiple in situ and remote sensing measurements and a large-eddy simulation (LES) model coupled with a chemical module. Our study area is Huntsville AL USA, a typical midsize city in the Southeastern United States. The ozone variation in the convective boundary layer (CBL) was mainly caused by local emissions and photochemical production due to weather conditions controlled by an anticyclonic system on that day. The local chemical production contributes over 2/3 of the ozone enhancement in the CBL. Dynamical processes, including ozone transport from the free troposphere (FT) to the CBL through the entrainment processes, contribute the remainder. The numerical experiments performed by the LES model show good agreement with ozone DIAL observations. This study indicates a need for fine-scale, three-dimensional ozone observations with high temporal and spatial resolution for air quality studies at urban and smaller scales.

Keywords: convective boundary layer, ozone, lidar, large-eddy simulation

1. Introduction

Ozone is one of the most important air pollutants due to its harmful effects on human health, agriculture, forests, and material damage [*EPA*, 2008; *Jenkin and Clemitshaw*, 2000]. Generally, ozone variations in the convective boundary layer (CBL) are associated with multiple factors such as surface emission and deposition, interaction with the free-troposphere (FT), and transport, in addition to the NOx(=NO+NO_2)-Volatile organic compounds(VOCs) chemical production with presence of sunlight [*Huang et al.*, 2015; *Jaffe and Wigder*, 2012; *Kuang et al.*, 2011b; *Kuang et al.*, 2012; *Langford et al.*, 2012; *Tong et al.*, 2011]. In the Southeastern United States, ozone concentrations are more sensitive to nitrogen oxides in rural areas due to the high VOC emissions from dense forest coverage. In urban areas (e.g., Atlanta, GA), ozone concentrations are sensitive to both nitrogen oxidants and VOCs from both anthropogenic and natural [*Blanchard et al.*, 2014; *Duncan et al.*, 2010]. Additionally, air stagnation regimes have more influence on the episode days than synoptic scale transport in the Southeastern United States [*Hidy*, 2000].

Ground ozone variation at small scales is receiving increasing concern due to the dramatically growing population [*Castellanos et al.*, 2011; *Shao et al.*, 2009; *So and Wang*, 2003; *Yegorova et al.*, 2011; *Y Zhang et al.*, 2012]. The urbanization processes can influence a wide range of the atmospheric flow, including the surface-air exchange, turbulence regime, the micro-climate, and accordingly change the transport, dispersion and deposition of atmospheric pollutants including ozone. NASA plans to launch a geostationary air-quality satellite, Tropospheric Emission: Monitoring of Pollution (TEMPO), providing high spatio-temporal observations [*Chance et al.*, 2013; *Zoogman et al.*, 2017]. Furthermore, air-quality studies with fine scales are one of the most important foci in recent field campaigns (e.g., DISCOVER-AQ field campaign, Deriving Information on Surface conditions from Column and Vertically Resolved Observations Relevant to Air Quality), SEAC^{4}S (Studies of Emissions and Atmospheric Composition, Clouds and Climate Coupling by Regional Surveys) [*Goldberg et al.*, 2014; *Martins et al.*, 2013; *Peterson et al.*, 2014].

Thorough knowledge of urban CBL structure is the key to satellite observations and forecast modeling of fine-scale air quality studies. However, studies of urban CBL structures are very challenging due to many factors such as the lack of fine resolution observations, emission and deposition inventories, and the coarse resolution of current air-quality models [*Castellanos et al.*, 2011; *Duncan et al.*, 2014; *J. Fishman et al.*, 2012; *Y Zhang et al.*, 2012]. Several studies have utilized, with considerable success, lidar measurements and large-eddy simulation (LES) model to study air quality with fine resolutions by taking advantage of the strengths of observations and simulations with fine resolution [*Chamecki et al.*, 2009; *Kuang et al.*, 2011b; *Langford et al.*, 2010; *Ouwersloot et al.*, 2012; *Senff et al.*, 2010; *van Stratum et al.*, 2012]. In this paper, we combine the strengths of the lidar and LES model for fine-scale urban air-quality studies to investigate impacts

of the CBL chemical and dynamical processes on ozone diurnal variation in Huntsville AL, a typical midsize city in the Southeastern United States.

The structure of this paper is as follows: Section 2 describes the measurements and models. Section 3 describes the methodology. Section 4 provides a discussion and analysis on the results. Section 5 summarizes and concludes this study.

2. Measurements and model

2.1. Measurements

Ozone production in Huntsville AL is more sensitive to NOx than VOCs because the Southeastern United States has dense forest coverage and agricultural land that emit significant VOCs in the summer, resulting in frequently elevated ozone levels [*Biazar*, 1995; *Blanchard et al.*, 2014]. Observations were collected on September 6, 2013 during the field campaign of Studies of Emissions and Atmospheric Composition, Clouds and Climate Coupling by Regional Surveys ($SEAC^4RS$), which included ozone and meteorological fields from multiple platform instruments located on the campus of University of Alabama in Huntsville (UAH 34.724°N, 86.645°W) [*Kuang et al.*, 2011b].

The tropospheric ozone Differential Absorption Lidar (DIAL) was developed jointly by the University of Alabama in Huntsville (UAH) and NASA Goddard Space Flight Center (GSFC). This DIAL retrieves ozone profiles, with a precision generally better than 10%, from 100 m AGL to ~10 km AGL with a temporal resolution of up to 2 minutes and a varied vertical resolution from 150 m at the bottom of the measurement range to 550 m at the top. Consequently, this DIAL can provide continuous ozone observations, which are used to study the ozone variation in the CBL [*Kuang et al.*, 2011a; *Kuang et al.*, 2013].

UAH's Mobile Integrated Profiling System (MIPS) is a collection of instruments located on UAH's campus, which is approximately 100 m from our ozone DIAL. It includes a 2kHz Doppler Sodar, a 915MHz Doppler wind profiler (Radian LAP-3000), a 12-channel microwave profiling radiometer (MPR, Radiometrics TP/WVP-3000), and a Vaisala laser ceilometer (Vaisala CT-41k), and surface instrumentation [*Busse and Knupp*, 2012; *Karan and Knupp*, 2006; *Knupp et al.*, 2009; *Wingo and Knupp*, 2014]. A recently acquired 1.5 μm Compact Wind and Aerosol Lidar (CWAL) is co-located in the same lab as our ozone DIAL. Table 1 lists a brief description of each instrument. A more detailed description of MIPS is available at http://vortex.nsstc.uah.edu/mips/system/.

3. Dutch Atmospheric Large-Eddy Simulation (DALES)

We use DALES 4.0 in this study. DALES is developed and maintained by Delft University of Technology, the Royal Netherlands Meteorological Institute, Wageningen University, Max Planck Institute for Chemistry, Utrecht University, and Technical University of Catalonia, etc. [*Böing et al.*, 2012; *Heus et al.*, 2010]. It has been used in studies of boundary layer dynamics and chemistry,

since it has the ability to couple the two together [*Aan de Brugh et al.*, 2013; *Ouwersloot*, 2013; *Ouwersloot et al.*, 2011; *Vilà-Guerau de Arellano et al.*, 2005]. This feature makes it possible for us to study ozone variations in the CBL through complex dynamical and chemical processes in fine resolutions [*Blay-Carreras et al.*, 2014; *van Stratum et al.*, 2012; *Vilà-Guerau de Arellano et al.*, 2009]. The processes with scales larger than a set filter width are explicitly resolved using the Navier-Stokes equation with the Boussinesq approximation while smaller-scale processes are parameterized based on a one and one-half order closure assumption. Periodic boundary conditions occur in all four horizontal directions in this study [*Heus et al.*, 2010].

One of the advantages of DALES is to explicitly resolve turbulence, including intensities of segregation. By resolving the turbulence and coupling it with the chemical solver, we can simultaneously solve the physics and chemistry equations; thereby, exposing their interactions within the CBL. Because simulating complex chemistry in the CBL is computationally expensive, we balance the costs between scientific fidelity and computational time. We chose a chemical mechanism that reproduces the essential components of the O_3-NOx-VOC-HOx system with the acceptable computational costs used in previous studies (see Table 2) [*Ouwersloot*, 2013; *Vilà-Guerau de Arellano et al.*, 2011; *Vilà-Guerau de Arellano et al.*, 2009]. The limited number of species and reactions results in a better understanding of the main chemical pathways. In addition, the degrees of freedom are reduced with less species, resulting in the model uncertainty from the initial and boundary conditions [*van Stratum et al.*, 2012].

Deposition is a large portion of the removal process of atmospheric chemicals from the CBL [*Wesely and Hicks*, 2000]. There are two major categories of deposition: wet deposition and dry deposition. Wet deposition is the natural process where trace chemicals are absorbed by hydrometeors and are brought to the Earth's surface through precipitation scavenging, cloud interception, fog deposition, and snow deposition [*Seinfeld and Pandis*, 2006]. Dry deposition is the transport of gaseous and particulate species from the atmosphere onto the Earth's surface without precipitation [*Biazar*, 1995; *Seinfeld and Pandis*, 2006]. Unfortunately, DALES does not include a dry deposition module. In order to estimate the dry deposition to the maximum extent, we add a module, which is described as follows:

We consider only dry deposition in this paper and assume the dry deposition flux is directly proportional to the local concentration of the depositing species at the reference height above the Earth's surface. The dry deposition flux can be written as:

$$\boldsymbol{F = -Vd[X]}, \qquad \textbf{Eq. 1}$$

where F is the dry deposition flux, $[X]$ is the concentration of deposition at the reference height above the surface and Vd is the deposition velocity. This empirical equation of dry deposition simplifies the complex chemical and physical processes of the dry deposition into one parameter, Vd.

The removal mechanism contains three steps. The first step is the transport of the gaseous and particulate species to the surface's vicinity by turbulent diffusion, which has a strong diurnal variation [*Stull*, 1988]. The second step involves the diffusion of the pollutant through the laminar sub-layer and contact with the surface. The Quasi-laminar sub-layer is a layer with thickness on the order of millimeters, adjacent to the Earth's surface, where the air is almost stationary. The third step is the removal of the gaseous and particulate species by the Earth's surface. Gaseous species may absorb irreversibly into the surface, and particles may simply adhere to the surface. The moisture in the surface is an important factor in this step. For a highly soluble species, the deposition is rapid [*Biazar*, 1995; *Seinfeld and Pandis*, 2006]. Each step contributes to the value of the deposition velocity; therefore, the dry deposition velocity, *Vd*, is a strong function of surface type and meteorology [*Dentener et al.*, 2014; *Erisman et al.*, 1994; *Ganzeveld and Lelieveld*, 1995; *Pleim et al.*, 2001; *L Zhang et al.*, 2003; *L Zhang et al.*, 2002].

The dry deposition velocity is inversely proportional to a resistant parameter *r*:

$$\boldsymbol{Vd \propto 1/r}. \qquad \textbf{Eq. 2}$$

Thus, the lower resistance will have a higher deposition velocity. In the deposition process in terms of an electrical resistance analogy, the resistance *r* can be considered the sum of two resistances: aerodynamic (r_a) and surface (or canopy) resistance (r_c). The aerodynamic resistance includes both resistances that a species exhibits in step one and two during the dry deposition processes. Meteorological conditions and atmospheric turbulence influence both steps. The aerodynamic resistance r_a can be written as:

$$\boldsymbol{r_a = \frac{\ln\left(\frac{z}{z_0}\right)+2.6-\Phi_H}{k\,u_*}}, \qquad \textbf{Eq. 3}$$

where *z* is the height of the first grid point above the Earth's surface, z_0 is the surface roughness, Φ_H is the non-dimensional temperature gradient, *k* (=0.35) is the von Karman's constant, and *u** is the friction velocity.

The final resistance in the dry deposition processes is the surface resistance r_s. The surface resistance depends on the tendency of the surface type to absorb certain materials. We used a surface resistance of 2 cm^{-1} for ozone, 0.1 s cm^{-1} for HNO_2, 2 s cm^{-1} for peroxides, and 3.3 s cm^{-1} for carbonyls and organic nitrates [*Biazar*, 1995]. The surface resistance of the other chemical species is set as $r_s = \frac{1}{V_{dmax}}$, where V_{dmax} is the maximum deposition velocity found in our literature review [*Biazar*, 1995; *Erisman et al.*, 1994; *Ganzeveld and Lelieveld*, 1995; *Sickles Ii and Shadwick*, 2015; *L Zhang et al.*, 2003]. Finally, the deposition velocity in the model is calculated according to the following equation:

$$\boldsymbol{V_d = \frac{1}{(r_a+r_s)}}. \quad \textbf{Eq. 4}$$

4. Methodology

4.1. Physics settings

The spatial resolution of the domain is set to 50m × 50m × 25m in x, y, and z directions, respectively, with 100 × 100 × 96 grid cells in each dimension; consequently, the simulation domain is 5km × 5km × 2.4km. The total simulation time is set to 10 hours with an adaptive time step of a maximum of 10 seconds, which avoids instabilities in the chemical solver and expensive computational costs. The fine temporal and spatial resolution resolves both atmospheric dynamical and chemical scales in the CBL. In order to lower the computational cost, we set the output intervals to 30 seconds.

To simulate the diurnal variation surface sensible and latent heat flux, both surface sensible and latent heat flux are set to 0.12×SIN (SIN=sin(π×(time-1380)/45803)) $K \cdot ms^{-1}$ and 0.0001×SIN $kg \cdot kg^{-1} \cdot ms^{-1}$, respectively, while the sunset time is 0523 UTC. The geostrophic winds are set to zero, and initial profiles of horizontal winds, potential temperature, and water vapor are obtained from the co-located MIPS measurements as shown in Figure 1. The first level meteorological data are obtained from surface measurements of MIPS. The ozone initial profiles are obtained from ozone DIAL, and the first level ozone input is obtained from the one-hour ozone mixing ratio at 1000 UTC measured at EPA air-quality station that is located 6 km south from the ozone DIAL.

4.2. Chemistry settings

The ozone chemistry that is typical for the Southeastern United States consists of very high VOC emissions due to the dense forest coverage. Therefore, ozone production is controlled by NOx concentration. According to the previous studies, the emission rate of isoprene and NO is set to 0.65×SIN and 0.08×COS (COS= (1-cos(π×(time-1380)/45803))) ppb/s, respectively [*Geron et al.*, 1997; *Kesselmeier and Staudt*, 1999; *Sullivan et al.*, 1996]. Table 3 shows the initial profiles of the chemical species. For comparison, we have two numerical experiments with 50% and 100% more NO emission for comparisons, one numerical experiment with turning off chemistry and dry deposition. Therefore, we have four numerical experiments with different NO emission rates as 0.08×COS ppb/s, 0.12× ppb/s NO, and 0.16×COS ppb/s, and control running with chemistry and dry deposition off, respectively.

5. Results and discussions

5.1. Meteorological analysis

It is well known that meteorological fields play a critical role in the formation, transport, and deposition of air pollutants [*Solomon et al.*, 2000]. The surface analysis of the weather chart at UTC 1200 on September 6, 2013 clearly indicates that weather conditions in Huntsville, AL were controlled by an anticyclonic system as shown in Panel (A) of Figure 2. As a result, the weather conditions in Huntsville AL were slightly windy with clear skies and no cloud coverage. The 10-m surface wind speed was very low with less than 2 ms^{-1} measured by surface instruments as

shown in the bottom of Panel (C). Wind profiles observed by 915-MHz indicates the low wind in the CBL and the slightly increased wind above the CBL top shown in Panel (B) of Figure 2. Solar radiation measured by the surface instruments in the top of Panel (C) of Figure 2 shows the diurnal curve of solar radiation without any interferences and the ceilometer did not detect any clouds on that day as shown in Panel (D). These weather conditions indicate that the ozone horizontal advection was too weak to transport the ozone amount to our study area, and the clear sky provides a large amount of solar radiation for photochemical reactions. Consequently, the ozone enhancement in the CBL on September 6, 2013 was mainly caused by local emissions.

5.2. The CBL height

The CBL height plays an important role in the ozone variation by diluting ozone concentrations and mixing air from the FT into the CBL through entrainment processes. We applied the continuous wavelet transform (CWT) algorithm to determine CBL heights based on the backscatter profile observed by CWAL with smoothing processes as plotted by the solid black line in Figure 3 [*Davis et al.*, 2000; *Huang et al.*, 2015]. In addition, the simulated CBL heights by DALES are plotted by the solid red line in Figure 3 as well. Generally, simulated CBL heights show good agreement with the observed CBL heights. The DALES model successfully reproduces the evolution of CBL heights in the early morning. However, the model underestimates the CBL height between 1600 and 1700 UTC when a residual layer storing high aerosol concentrations at a 1.2 – 1.4 km height is incorporated into the growing CBL. The residual layer usually involves mean characteristics of the previous CBL including air pollutants, potential temperatures, and relative humidity, etc. When the potential temperature in the CBL reaches the potential temperature in the RL, the CBL grows extremely fast by engulfing the residual layer, since no (significant) inversion is present anymore between the growing CBL and the RL [*Ouwersloot et al.*, 2012]. Consequently, the CBL height jump between 1600 and 1700 UTC is not captured by the DALES model. Moreover, the diurnal variation of large-scale subsidence causes the CBL underestimation after 1800 UTC [*Blanchard et al.*, 2014].

5.3. Ozone variation in the CBL

In order to study ozone redistribution by eddy transport in the CBL without smoothing out the turbulence information, we investigate the ozone profiles at the center grid point of our domain with a 50 m horizontal and 25 m vertical resolution. The ozone observations from the ozone DIAL, simulation by DALES with standard NO emissions are plotted in Figure 4 from the top to the bottom panels, respectively. DALES reproduces the ozone temporal variation and the ozone structure caused by eddies in the CBL as shown in the top and middle panels in Figure 4. DALES reproduces the ozone variation and ozone morphology caused by eddies in the CBL as shown in the middle panel of Figure 4. The ozone simulation of control running with chemistry off in the

bottom panel of Figure 4 implies that the ozone temporal variation on September 6, 2013 was caused mainly by local emissions and chemical production.

To quantify the comparisons between the ozone simulations and observations, we compared the model simulations with the observations between 0.1 and 2.475 km AGL in Figure 5. The top panel is ozone scattering plots of ozone DIAL and standard NO emission simulation, while we also compare the simulation of DALE control running with the same physical settings and turning chemical setting off. The comparison plot of control run versus observations in the bottom panel in Figure 6 shows two high number density patterns at (45, 65) and (52, 52) at the coordinates. The high-density pattern at (52, 52) shows good agreement of observed and simulated ozone in the FT since the ozone in the FT does not change in this case. The other high-density patterns at (45, 65) are the CBL ozone that the control run underestimates due to the lack of chemistry mechanisms. The simulated ozone with standard NO emission indicates a good agreement with the DIAL-observed ozone.

Figure 6 plots the CBL ozone mixing ratios obtained by in situ and remote sensing observations along with the model simulations. Note that all CBL ozone mixing ratios are averaged over the whole domain to remove high frequent noises. This is helpful to compare with the hourly ozone surface measurements. The blue dashed-dot, dashed, and solid lines represent the CBL ozone mixing ratio modeled with 200% NO emission simulation, 150% more NO emission and standard NO emission, respectively. The modeled CBL ozone mixing ratio is highly associated with NO emission in the sunlight presence. The average ozone production rates in the CBL are 3.8ppb/hour, 4.2ppb/hour and 4.5ppb/hour for standard, 150% and 200% NO emissions, respectively. The red dashed and solid lines represent the ozone mixing ratio at 100 m AGL (the minimum height that ozone can be measured) and CBL ozone mixing ratio observed by ozone DIAL. Ozone mixing ratio simulated with standard NO emission (solid blue line) has a good agreement with ozone observations at 100 m AGL. Both of them capture the increased trend of ozone during the daytime. However, DALES underestimates the CBL ozone plotted by the solid red line in Figure 7. This underestimation is probably caused by the overestimation of the CBL height that involves the lower FT with low ozone, especially after 1800 UTC. Additionally, the CBL ozone simulated with chemistry off, plotted by a solid gray line, shows a slight ozone increase in the CBL due to the mixing of ozone in the FT through entrainment processes. The chemical productions contribute over 2/3 to the total CBL ozone budget and the dynamical transports contribute the rest based on these simulations.

5.4. Ozone transport within the CBL

Ozone transport within the CBL is a significant process for both ground ozone concentrations and the CBL budget. The land surface can provide either a strong ozone sink by deposition processes or a strong ozone production source through high emissions. The redistribution of ozone in the CBL occurs through convective mixing; the interaction between the CBL and the ground ozone

concentration occurs through turbulent flux. For the calculation of the turbulence's impacts on ozone, we need to investigate the highly-resolved time series of vertical wind velocity and aerosol scattering data at specific height levels. We apply Taylor's frozen turbulence hypothesis: it is assumed that the temporally-resolved dataset will represent the spatial ensemble average. Then, the turbulent ozone flux is defined as $\overline{w'O_3'}$, where the prime represents deviations from the mean value, and the overbar represents the temporal average.

The vertical wind profiles observed by CWAL are plotted in Figure 8. After the sunrise, eddies start to grow vertically due to the increasing surface heat flux as shown in Figure 8. A layer stays at approximately 300 m AGL through our observations. We believe this layer is at least due to some local effect. This persistence through our observation period suggests a possible remnant warm plume atop the relatively warmer building and more urbanized area around the campus [*Wingo and Knupp*, 2014].

The statistical errors of the ozone flux due to noise have been taken into account. The measured ozone flux is written as [*Senff et al.*, 1996]:

$$\overline{\boldsymbol{w'O_3'}}_{\boldsymbol{m}} = \overline{\boldsymbol{w'O_3'}} + \overline{\boldsymbol{\delta w'O_3'}} + \overline{\boldsymbol{w'\delta O_3'}} + \overline{\boldsymbol{\delta w'\delta O_3'}}, \qquad \textbf{Eq. 5}$$

where δw' and δO_3' is fluctuations of vertical wind and ozone mixing ratio, respectively. The variance of the measured ozone flux caused by system noise can be expressed as [*Senff et al.*, 1996]:

$$\begin{aligned}
&\boldsymbol{\sigma^2}\left(\overline{\boldsymbol{w'O_3'}}_{\boldsymbol{m}}\right) = \boldsymbol{\sigma^2}\left(\overline{\boldsymbol{\delta w'O_3'}} + \overline{\boldsymbol{w'\delta O_3'}} + \overline{\boldsymbol{\delta w'\delta O_3'}}\right),\\
&= \boldsymbol{E}\left(\overline{\boldsymbol{\delta w'O_3'}}^{\boldsymbol{2}} + \overline{\boldsymbol{w'\delta O_3'}}^{\boldsymbol{2}} + \overline{\boldsymbol{\delta w'\delta O_3'}}^{\boldsymbol{2}}\right),\\
&= \frac{\boldsymbol{1}}{\boldsymbol{N}}\left(\overline{\boldsymbol{O_3'}}^{\boldsymbol{2}}\,\overline{\boldsymbol{\delta^2 w'}} + \overline{\boldsymbol{\delta^2 O_3'}}\,\overline{\boldsymbol{w'}}^{\boldsymbol{2}} + \overline{\boldsymbol{\delta^2 O_3'}}\,\overline{\boldsymbol{\delta^2 w'}}\right),\\
&= \frac{\boldsymbol{1}}{\boldsymbol{N}}\left(\overline{\boldsymbol{O_3'}}^{\boldsymbol{2}}_{\boldsymbol{m}}\,\overline{\boldsymbol{\delta^2 w'}} + \overline{\boldsymbol{\delta^2 O_3'}}\,\overline{\boldsymbol{w'}}^{\boldsymbol{2}}_{\boldsymbol{m}} + \overline{\boldsymbol{\delta^2 O_3'}}\,\overline{\boldsymbol{\delta^2 w'}}\right). \qquad \text{Eq. 6}
\end{aligned}$$

We calculate the observed ozone turbulent flux (solid black line) with statistical errors at each level (horizontal black line) every 30 minutes from 1700-200 UTC in Figure 8, as well as the simulated ozone turbulent flux(solid red line). It is obvious that the spatial and temporal resolutions of ozone DIAL and CWAL are not fine enough to capture the ozone flux caused by small eddies (length less than measurement resolution). Consequently, ozone flux may be underestimated. However, the ignored portion of the ozone flux should be negligible in the convective boundary layer. The unresolved part of the ozone flux cannot be quantified since there is no in situ measurement on both ozone and wind with high resolution for comparing with the measurements by ground-based remote-sensing techniques [*Patton et al.*, 2005].

The statistical errors are significantly larger at approximately 200-500m AGL for each panel in Figure 8, possibly because of a remnant warm plume from the relatively warmer building and more urbanized area around the campus[*Wingo and Knupp*, 2014]. The majority of the simulated ozone fluxes above 500 m AGL are within the range of observed ozone fluxes plus or minus statistical errors. This indicates that DALES reproduces the typical ozone behavior for a clear late summer day: the CBL ozone mixing ratio increases during the daytime due to local production with the

sunlight presence. Figure 2 shows a RL at 1600- 1700 UTC stores low ozone. The knowledge of the vertical distribution of the ozone mixing ratio in the CBL and RL allows some basic predictions about the turbulent fluxes associated with this ozone vertical distribution. The ground is known to be an ozone sink due to the dry deposition, while the photochemical production of ozone in the CBL under clear summer conditions acts as a source of ozone. This causes slightly higher ozone mixing ratio in the CBL than at the ground surface. Therefore, observed ozone fluxes indicate downward motion in each time interval.

6. Conclusion

We investigated the ozone diurnal evolution on September 6, 2013 in Huntsville, AL using multiple measurements and the DALES model coupled with a chemical module. DALES successfully reproduced the CBL ozone enhancement due to local emissions and chemical productions. The comparison experiments between chemical and control-running (with chemistry off) of the model suggest that the ozone production was controlled by local emissions in this particular day with low horizontal winds and strong solar insolation. This study indicates that LES model and Lidar observations, in high temporal and spatial resolution, are powerful tools to help us understand the ozone and other air pollutant variations in the CBL.

The CBL height is determined by finding the highest gradients in the CWAL backscatter profiles using the continuous wavelet transform technique. Generally, DALES-simulated CBL heights have good agreement with the observed CBL heights. The two reasons that the model misrepresented the CBL heights are the intrusion of the RL and the variation of large-scale subsidence. A RL storing low ozone concentration is incorporated into the growing CBL that results in a CBL height jump due to the free encroachment processes. The large-scale subsidence is treated as a downward motion constant in DALES. Consequently, DALES misses the variation of large-scale subsidence leading to CBL heights being overestimated.

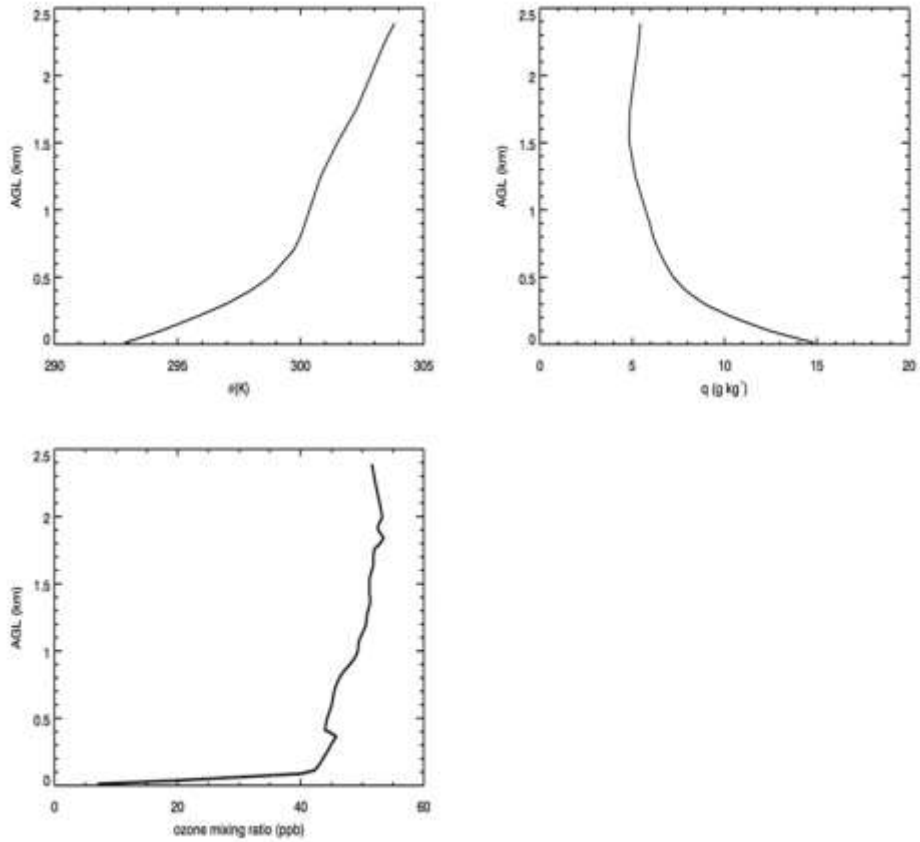

Figure 1 Initial profiles of potential temperature, water vapor, and ozone mixing ratio. The 1-hour averaged ozone profiles is provided by ozone DIAL except for the surface value which sourced from the Huntsville EAP station 6km away from the DIAL lab.

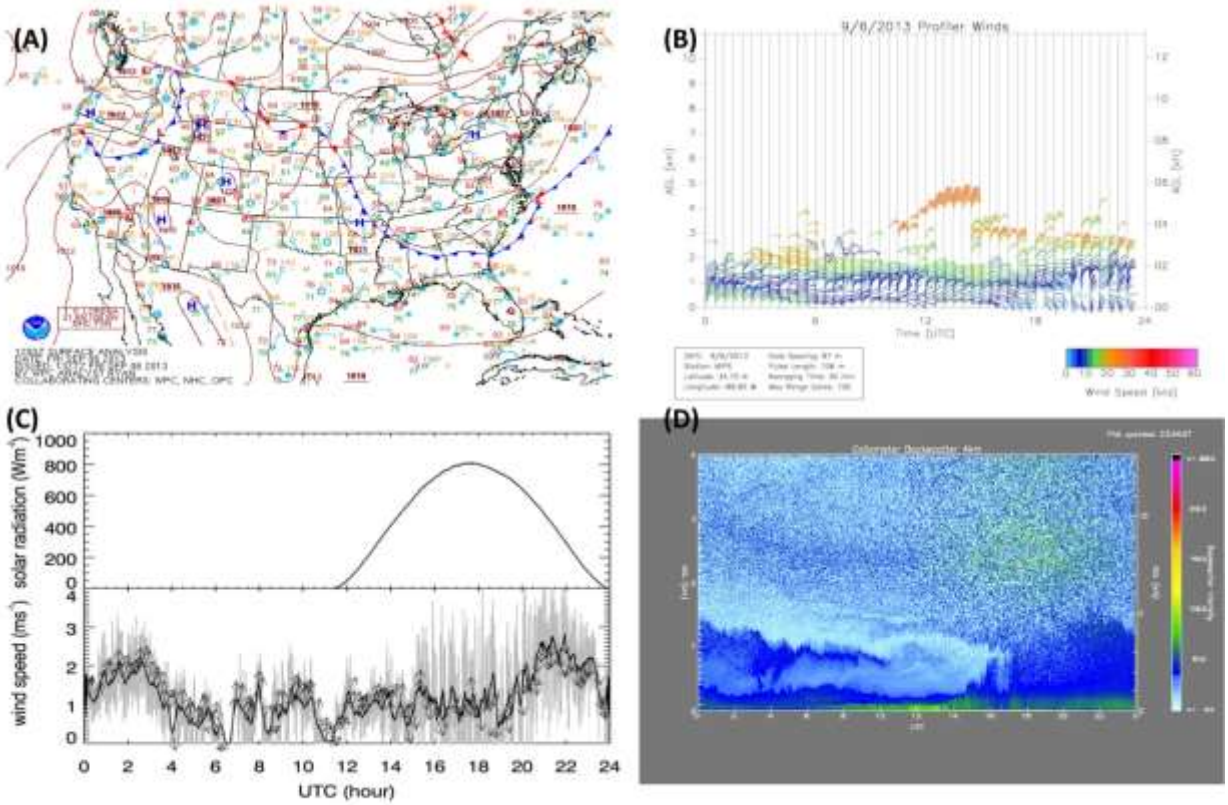

Figure 2 Weather chart and micro-meteorological measurements on September 6, 2013 in Huntsville, AL. (a) Weather charts at 1200z on September 6, 2013 from NOAA National Climatic Data Center (http://nomads.ncdc.noaa.gov/ncep/NCEP), (b) Wind velocities measured by 915MHz wind profiler, (c) Solar radiation and surface wind measured by surface instruments, and (d) Backscatter measured by the ceilometer.

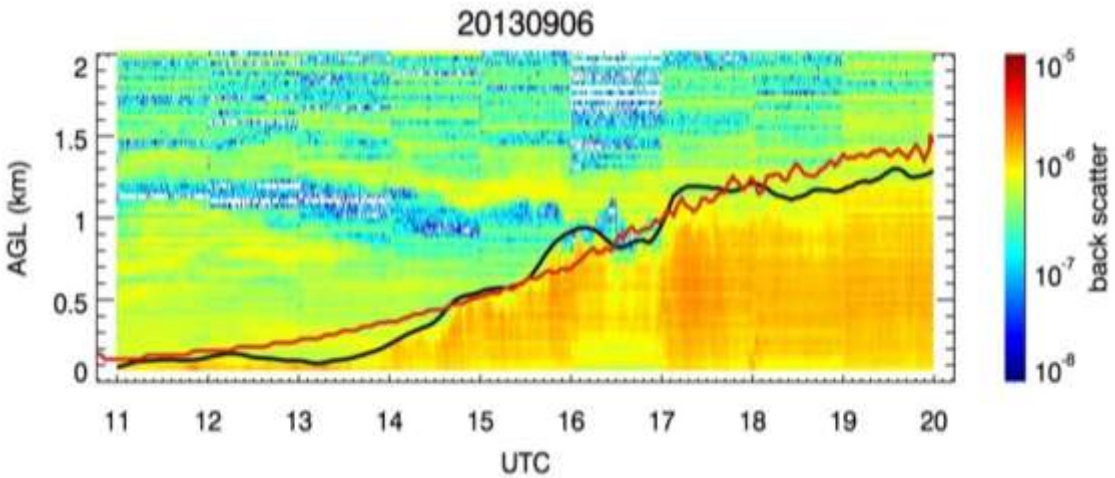

Figure 3 Backscatter observed by CWAL at Huntsville, AL. The solid black line represents the CBL height obtained based on the backscatter profile and the solid red line represents the CBL height simulated from DALES.

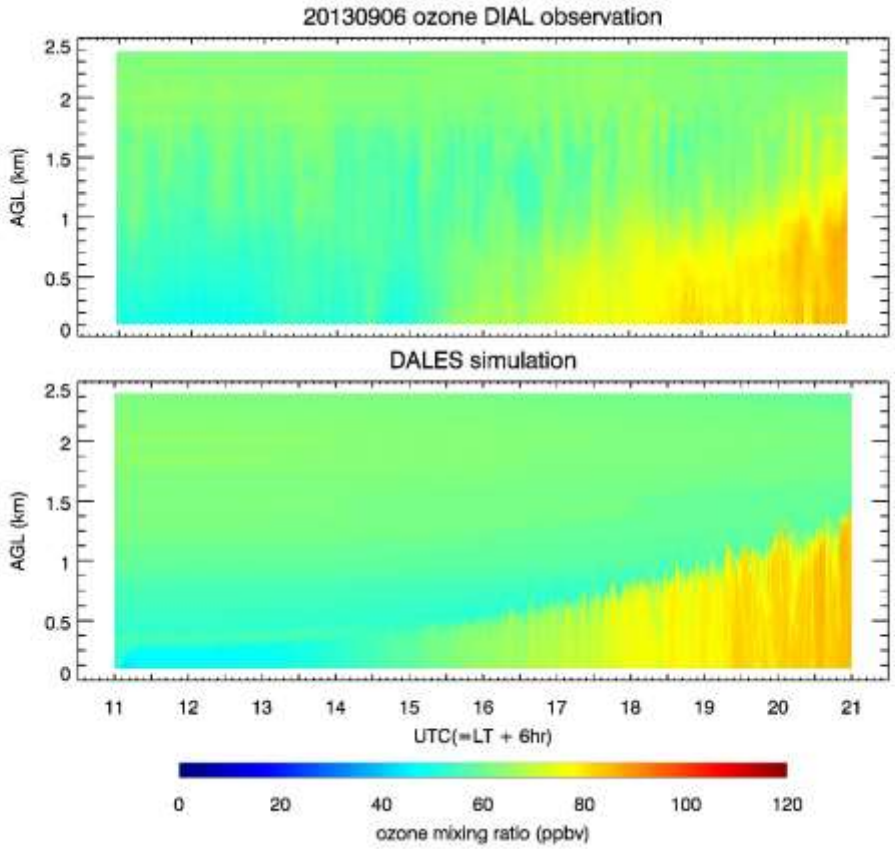

Figure 4 Ozone mixing ratio profiles measured by ozone DIAL and ozone mixing ratio at the center grid of the entire domain simulated by DALES. The top and bottom panels are ozone profiles measured by ozone DIAL, simulated by DALES with chemistry running, respectively.

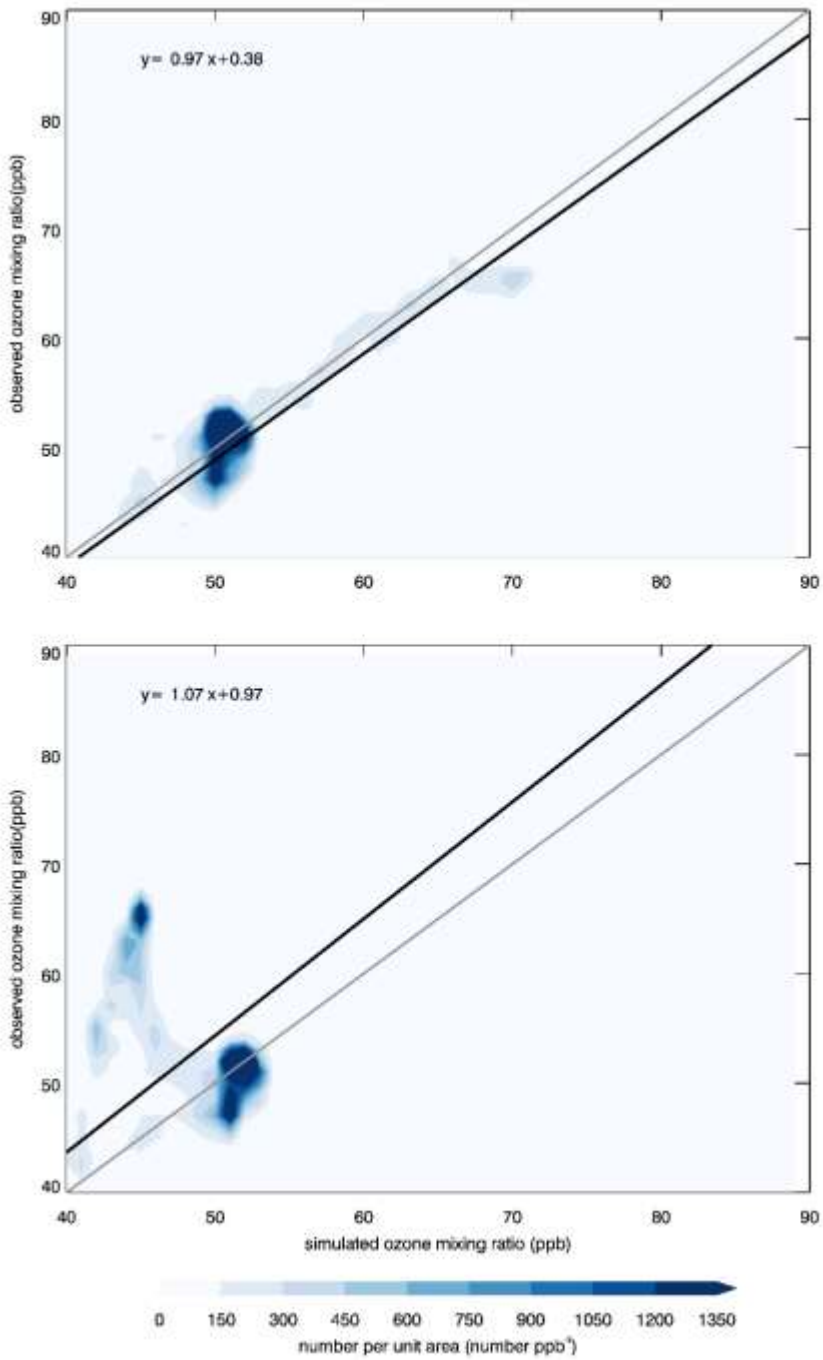

Figure 5 The scattering plot of observed and simulated ozone. The top and bottom panels represent standard run vs. observations and control run vs. observations, respectively. The black lines are the linear regression fitting function, and the gray lines are y=x function.

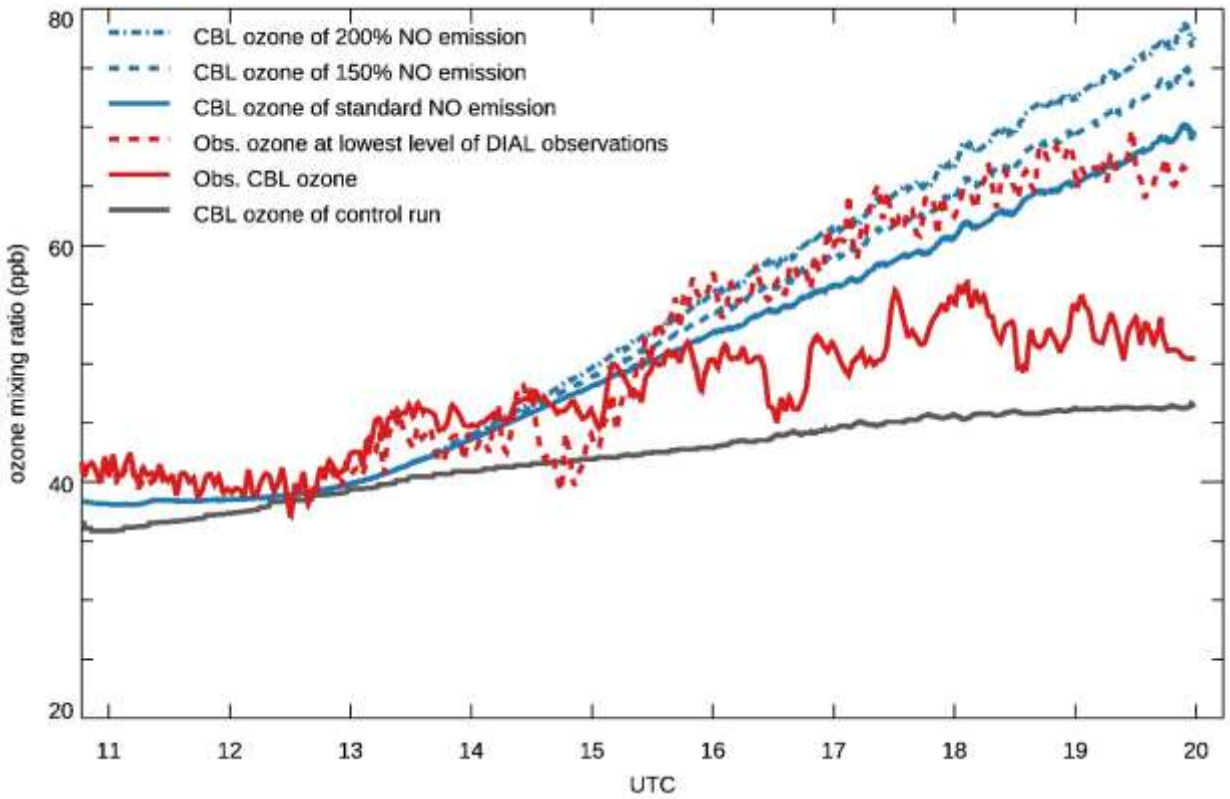

Figure 6 Observed and simulated CBL ozone variations. The blue dashed-dotted, dashed and solid lines are simulated CBL ozone with 100% more NO emission, 50% more NO emissions and standard NO emissions, respectively. The red dashed and solid lines represent, respectively, ozone mixing ratio the lowest level of ozone DIAL observations and CBL ozone observed by ozone DIAL. The solid gray line represents CBL ozone simulated by the control run.

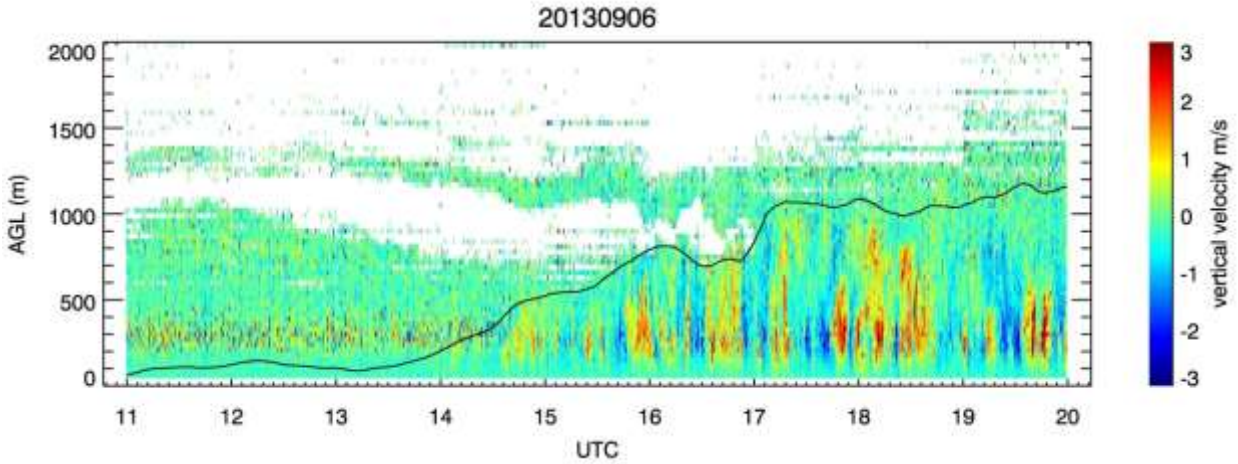

Figure 7 Vertical wind velocity measured by CWAL. The positive and negative values represent upward and downward motion, respectively.

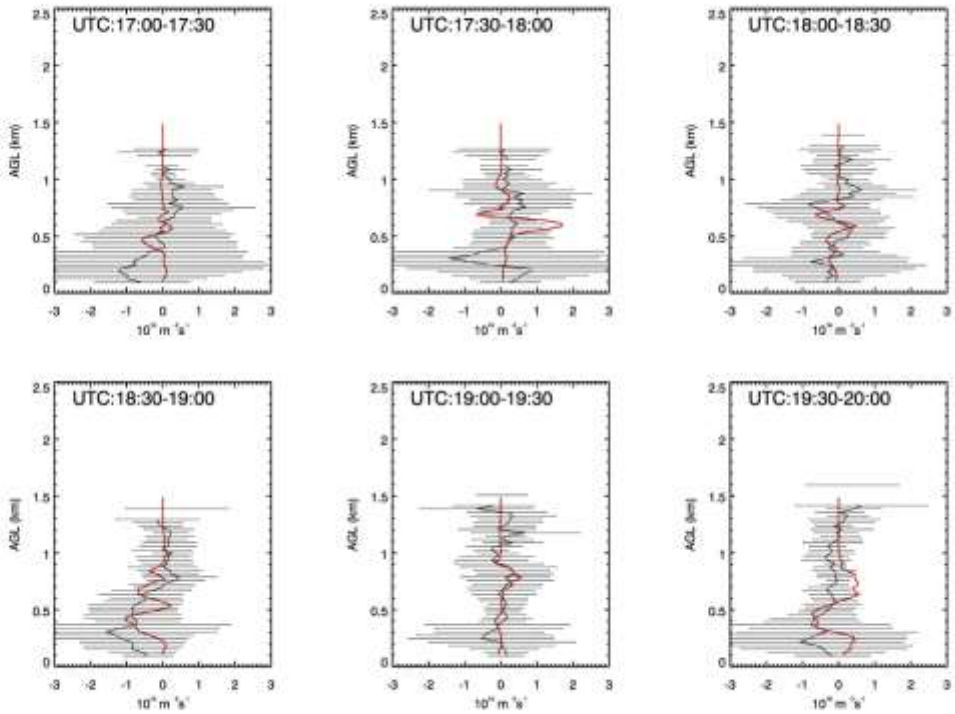

Figure 8 The solid black line represents the observed ozone turbulence flux with statistical error at each level shown in horizontal black line. The solid red line represents simulated ozone turbulence flux with standard NO emission at corresponding six intervals.

Table 1 Instrument descriptions

Instrument	Measurements	Vertical range	Vertical Resolution	Temporal Resolution
915 MHz wind profiler	vertical motion horizontal wind spectral width	0.19 - 4 km	60 or 106 m	60s
Ceilometer	backscatter cloud base	0.3 -10+km	30 m	15s
MPR	Temperature, integrated water vapor	surface - 10 km	100 m from surface to 1km 250m above 1km	1-14min
Ozone DIAL	Ozone	surface - 10+ km	30 m (sampling resolution)	2-10 min
CWAL	aerosol, wind velocity	0.75 -10 km	30 m	0.1-30 s
Surface	Temperature, wind velocity solar radiation	2m	N/A	5s

Table 2 Chemical reaction scheme solved in the numerical experiments by the chemical module of DALES. T is the absolute temperature in K. Product represents the reactants in the ambient air that are not directly evaluated.

Reaction Number	Reaction	Reaction Rate
R1	O3+hv → O(1D) + O2	$3.83 \times 10^{-5} \cdot e^{-\frac{0.575}{\cos(\chi)}}$
R2	O(1D) + H2O →2OH	$1.63 \times 10^{-10} \cdot e^{\frac{60}{T}}$
R3	O(1D) + N2 →O3 + PRODUCT	$2.15 \times 10^{-11} \cdot e^{\frac{110}{T}}$
R4	O(1D) + O2 →O3 + PRODUCT	$3.30 \times 10^{-11} \cdot e^{\frac{55}{T}}$
R5	NO2 +hv →NO + O3	$1.67 \times 10^{-2} \cdot e^{-\frac{0.575}{\cos(\chi)}}$
R6	CH2O +hv →HO2	$1.47 \times 10^{-4} \cdot e^{-\frac{0.575}{\cos(\chi)}}$
R7	OH +CO →HO2 CO2	2.40×10^{-13}
R8	OH + CH4→ CH3O2	$2.45 \times 10^{-12} \cdot e^{-\frac{1775}{T}}$
R9	OH + ISO →RO2	1.00×10^{-10}
R10	OH + MVK → HO2 +CH2O	2.40×10^{-11}
R11	HO2+NO → OH+NO2	$3.5 \times 10^{-12} \cdot e^{-\frac{250}{T}}$
R12	CH3O2+NO → HO2+NO2+CH2O	$2.8 \times 10^{-12} \cdot e^{-\frac{300}{T}}$
R13	RO2+NO →HO2+NO2+CH2O+MVK	1.00×10^{-11}
R14	OH + CH2O + O2 → HO2 + CO +H2O	$5.5 \times 10^{-12} \cdot e^{\frac{125}{T}}$
R15	HO2+HO2 → H2O2+O2	k*
R16	CH3O2 + HO2 →PRODUCT	$4.10 \times 10^{-13} \cdot e^{\frac{750}{T}}$
R17	RO2 + HO2 →nOH product	1.50×10^{-11}
R18	OH + NO2→ HNO3	$3.50 \times 10^{-12} \cdot e^{\frac{340}{T}}$
R19	NO + O3 →NO2 +O2	$3.00 \times 10^{-12} \cdot e^{-\frac{1500}{T}}$

k*=(k1+k2)·k3

$k_1 = 2.2 \times 10^{-13} \cdot e^{\frac{600}{T}}$ $\quad k_2 = 1.9 \times 10^{-33} \cdot e^{\frac{980}{T}} \cdot c_{air}$ $\quad k_3 = 1 + 1.4 \times 10^{-21} \cdot e^{\frac{2200}{T}} \cdot ch_{20}$

Table 3 Initial inputs of reactive chemicals for all four cases. The rest of the chemical species are set to zero.

	mixing ratio (ppb, z < 200m)	mixing ratio (ppb, z> 200m)
Ozone	as Figure 1	as Figure 1
NO	0	0
NO2	1	0
ISO	2	0
HO2	0	0
OH	0	0
MVK	1.3	1.3
CH4	1724	1724
CO	124	124

References

Aan de Brugh, J. M. J., H. G. Ouwersloot, J. Vilà-Guerau de Arellano, and M. C. Krol (2013), A large-eddy simulation of the phase transition of ammonium nitrate in a convective boundary layer, *J. Geophys. Res.-Atmos.*, *118*(2), 826-836, doi:10.1002/jgrd.50161.

Biazar, A. P. (1995), The role of natural nitrogen oxides in ozone production in the southeastern environment, Ph.D. thesis, 271-271 p. pp, The University of Alabama in Huntsville, Ann Arbor.

Blanchard, C. L., G. M. Hidy, and S. Tanenbaum (2014), Ozone in the southeastern United States: An observation-based model using measurements from the SEARCH network, *Atmos. Environ.*, *88*(0), 192-200, doi:10.1016/j.atmosenv.2014.02.006.

Blay-Carreras, E., D. Pino, J. Vilà-Guerau de Arellano, A. van de Boer, O. De Coster, C. Darbieu, O. Hartogensis, F. Lohou, M. Lothon, and H. Pietersen (2014), Role of the residual layer and large-scale subsidence on the development and evolution of the convective boundary layer, *Atmos. Chem. Phys.*, *14*(9), 4515-4530, doi:10.5194/acp-14-4515-2014.

Böing, S. J., H. J. J. Jonker, A. P. Siebesma, and W. W. Grabowski (2012), Influence of the Subcloud Layer on the Development of a Deep Convective Ensemble, *Journal of the Atmospheric Sciences*, *69*(9), 2682-2698, doi:10.1175/jas-d-11-0317.1.

Busse, J., and K. Knupp (2012), Observed Characteristics of the Afternoon–Evening Boundary Layer Transition Based on Sodar and Surface Data, *Journal of Applied Meteorology and Climatology*, *51*(3), 571-582, doi:10.1175/2011jamc2607.1.

Castellanos, P., L. T. Marufu, B. G. Doddridge, B. F. Taubman, J. J. Schwab, J. C. Hains, S. H. Ehrman, and R. R. Dickerson (2011), Ozone, oxides of nitrogen, and carbon monoxide during pollution events over the eastern United States: An evaluation of emissions and vertical mixing, *J. Geophys. Res.-Atmos.*, *116*(D16), D16307, doi:10.1029/2010JD014540.

Chamecki, M., C. Meneveau, and M. B. Parlange (2009), Large eddy simulation of pollen transport in the atmospheric boundary layer, *Journal of Aerosol Science*, *40*(3), 241-255, doi:http://dx.doi.org/10.1016/j.jaerosci.2008.11.004.

Chance, K., X. Liu, R. M. Suleiman, D. E. Flittner, J. Al-Saadi, and S. J. Janz (2013), Tropospheric emissions: monitoring of pollution (TEMPO).

Davis, K. J., N. Gamage, C. R. Hagelberg, C. Kiemle, D. H. Lenschow, and P. P. Sullivan (2000), An Objective Method for Deriving Atmospheric Structure from Airborne Lidar Observations, *Journal of Atmospheric and Oceanic Technology*, *17*(11), 1455-1468, doi:10.1175/1520-0426(2000)017<1455:AOMFDA>2.0.CO;2.

Dentener, F., R. Vet, R. L. Dennis, E. Du, U. C. Kulshrestha, and C. Galy-Lacaux (2014), Progress in Monitoring and Modelling Estimates of Nitrogen Deposition at Local, Regional and Global Scales, in *Nitrogen Deposition, Critical Loads and Biodiversity*, edited by M. A. Sutton, K. E. Mason, L. J. Sheppard, H. Sverdrup, R. Haeuber and W. K. Hicks, pp. 7-22, Springer Netherlands, doi:10.1007/978-94-007-7939-6_2.

Duncan, B. N., et al. (2014), Satellite data of atmospheric pollution for U.S. air quality applications: Examples of applications, summary of data end-user resources, answers to FAQs, and common mistakes to avoid, *Atmos. Environ.*, *94*(0), 647-662, doi:10.1016/j.atmosenv.2014.05.061.

Duncan, B. N., et al. (2010), Application of OMI observations to a space-based indicator of NOx and VOC controls on surface ozone formation, *Atmos. Environ.*, *44*(18), 2213-2223, doi:10.1016/j.atmosenv.2010.03.010.

EPA (2008), EPA's reports on the environment, edited by U. S. E. P. Agency, p. 366.

Erisman, J. W., A. Van Pul, and P. Wyers (1994), Parametrization of surface resistance for the quantification of atmospheric deposition of acidifying pollutants and ozone, *Atmos. Environ.*, *28*(16), 2595-2607, doi:10.1016/1352-2310(94)90433-2.

Fishman, J., et al. (2012), The United States' Next Generation of Atmospheric Composition and Coastal Ecosystem Measurements: NASA's Geostationary Coastal and Air Pollution Events (GEO-CAPE) Mission, *Bulletin of the American Meteorological Society*, *93*(10), 1547-1566, doi:10.1175/bams-d-11-00201.1.

Fishman, J., M. L. Silverman, J. H. Crawford, and J. K. Creilson (2011), A study of regional-scale variability of in situ and model-generated tropospheric trace gases: Insights into observational requirements for a satellite in geostationary orbit, *Atmos. Environ.*, *45*(27), 4682-4694, doi:http://dx.doi.org/10.1016/j.atmosenv.2011.05.008.

Ganzeveld, L., and J. Lelieveld (1995), Dry deposition parameterization in a chemistry general circulation model and its influence on the distribution of reactive trace gases, *J. Geophys. Res.*, *100*(D10), 20999, doi:10.1029/95jd02266.

Geron, C. D., D. Nie, R. R. Arnts, T. D. Sharkey, E. L. Singsaas, P. J. Vanderveer, A. Guenther, J. E. Sickles, and T. E. Kleindienst (1997), Biogenic isoprene emission: Model evaluation in a southeastern United States bottomland deciduous forest, *Journal of Geophysical Research*, *102*(D15), 18889, doi:10.1029/97jd00968.

Goldberg, D. L., C. P. Loughner, M. Tzortziou, J. W. Stehr, K. E. Pickering, L. T. Marufu, and R. R. Dickerson (2014), Higher surface ozone concentrations over the Chesapeake Bay than over the adjacent land: Observations and models from the DISCOVER-AQ and CBODAQ campaigns, *Atmos. Environ.*, *84*(0), 9-19, doi:http://dx.doi.org/10.1016/j.atmosenv.2013.11.008.

Heus, T., et al. (2010), Formulation of the Dutch Atmospheric Large-Eddy Simulation (DALES) and overview of its applications, *Geoscientific Model Development*, *3*(2), 415-444, doi:10.5194/gmd-3-415-2010.

Hidy, G. M. (2000), Ozone process insights from field experiments – part I: overview, *Atmos. Environ.*, *34*(12–14), 2001-2022, doi:http://dx.doi.org/10.1016/S1352-2310(99)00456-2.

Huang, G., M. J. Newchurch, S. Kuang, P. I. Buckley, W. Cantrell, and L. Wang (2015), Definition and determination of ozone laminae using Continuous Wavelet Transform (CWT) analysis, *Atmos. Environ.*, *104*(0), 125-131, doi:10.1016/j.atmosenv.2014.12.027.

Jaffe, D. A., and N. L. Wigder (2012), Ozone production from wildfires: A critical review, *Atmos. Environ.*, *51*(0), 1-10, doi:http://dx.doi.org/10.1016/j.atmosenv.2011.11.063.

Jenkin, M. E., and K. C. Clemitshaw (2000), Ozone and other secondary photochemical pollutants: chemical processes governing their formation in the planetary boundary layer, *Atmos. Environ.*, *34*(16), 2499-2527, doi:10.1016/s1352-2310(99)00478-1.

Karan, H., and K. Knupp (2006), Mobile Integrated Profiler System (MIPS) Observations of Low-Level Convergent Boundaries during IHOP, *Monthly Weather Review*, *134*(1), 92-112.

Kesselmeier, J., and M. Staudt (1999), Biogenic volatile organic compounds (VOC): An overview on emission, physiology and ecology, *J. Atmos. Chem.*, *33*(1), 23-88, doi:10.1023/A:1006127516791.

Knupp, K. R., T. Coleman, D. Phillips, R. Ware, D. Cimini, F. Vandenberghe, J. Vivekanandan, and E. Westwater (2009), Ground-Based Passive Microwave Profiling during Dynamic Weather Conditions, *Journal of Atmospheric and Oceanic Technology*, *26*(6), 1057-1073, doi:10.1175/2008JTECHA1150.1.

Kuang, S., J. F. Burris, M. J. Newchurch, S. Johnson, and S. Long (2011a), Differential Absorption Lidar to Measure Subhourly Variation of Tropospheric Ozone Profiles, *IEEE T. Geosci. Remote.*, *49*(1), 557-571, doi:10.1109/tgrs.2010.2054834.

Kuang, S., M. J. Newchurch, J. Burris, and X. Liu (2013), Ground-based lidar for atmospheric boundary layer ozone measurements, *Appl Opt*, *52*(15), 3557-3566, doi:10.1364/AO.52.003557.

Kuang, S., M. J. Newchurch, J. Burris, L. Wang, P. I. Buckley, S. Johnson, K. Knupp, G. Huang, D. Phillips, and W. Cantrell (2011b), Nocturnal ozone enhancement in the lower troposphere observed by lidar, *Atmos. Environ.*, *45*(33), 6078-6084, doi:10.1016/j.atmosenv.2011.07.038.

Kuang, S., M. J. Newchurch, J. Burris, L. Wang, K. Knupp, and G. Huang (2012), Stratosphere-to-troposphere transport revealed by ground-based lidar and ozonesonde at a midlatitude site, *J. Geophys. Res.-Atmos.*, *117*(D18), n/a-n/a, doi:10.1029/2012jd017695.

Langford, A. O., J. Brioude, O. R. Cooper, C. J. Senff, R. J. Alvarez, II, R. M. Hardesty, B. J. Johnson, and S. J. Oltmans (2012), Stratospheric influence on surface ozone in the Los Angeles area during late spring and early summer of 2010, *J. Geophys. Res.*, *117*, D00V06.

Langford, A. O., S. C. Tucker, C. J. Senff, R. M. Banta, W. A. Brewer, R. J. Alvarez, II, R. M. Hardesty, B. M. Lerner, and E. J. Williams (2010), Convective venting and surface ozone in Houston during TexAQS 2006, *J. Geophys. Res.*, *115*(D16), D16305.

Martins, D. K., R. M. Stauffer, A. M. Thompson, H. S. Halliday, D. Kollonige, E. Joseph, and A. J. Weinheimer (2013), Ozone correlations between mid-tropospheric partial columns and the near-surface at two mid-atlantic sites during the DISCOVER-AQ campaign in July 2011, *J. Atmos. Chem.*, 1-19, doi:10.1007/s10874-013-9259-4.

Ouwersloot, H. G. (2013), The impact of dynamic processes on chemistry in atmospheric boundary layers over tropical and boreal forest, Wageningen University, Wageningen.

Ouwersloot, H. G., J. Vilà-Guerau de Arellano, A. C. Nölscher, M. C. Krol, L. N. Ganzeveld, C. Breitenberger, I. Mammarella, J. Williams, and J. Lelieveld (2012), Characterization of a boreal convective boundary layer and its impact on atmospheric chemistry during HUMPPA-COPEC-2010, *Atmos. Chem. Phys.*, *12*(19), 9335-9353, doi:10.5194/acp-12-9335-2012.

Ouwersloot, H. G., J. Vilà-Guerau de Arellano, C. C. van Heerwaarden, L. N. Ganzeveld, M. C. Krol, and J. Lelieveld (2011), On the segregation of chemical species in a clear boundary layer over heterogeneous land surfaces, *Atmos. Chem. Phys.*, *11*(20), 10681-10704, doi:10.5194/acp-11-10681-2011.

Patton, E. G., P. P. Sullivan, and C.-H. Moeng (2005), The Influence of Idealized Heterogeneity on Wet and Dry Planetary Boundary Layers Coupled to the Land Surface, *Journal of the Atmospheric Sciences*, *62*(7), 2078-2097, doi:10.1175/JAS3465.1.

Peterson, D. A., E. J. Hyer, J. R. Campbell, M. D. Fromm, J. W. Hair, C. F. Butler, and M. A. Fenn (2014), The 2013 Rim Fire: Implications for Predicting Extreme Fire Spread, Pyroconvection, and Smoke Emissions, *Bulletin of the American Meteorological Society*, 141104074432007, doi:10.1175/BAMS-D-14-00060.1.

Pleim, J. E., A. Xiu, P. L. Finkelstein, and T. L. Otte (2001), A Coupled Land-Surface and Dry Deposition Model and Comparison to Field Measurements of Surface Heat, Moisture, and Ozone Fluxes, *Water, Air and Soil Pollution: Focus*, *1*(5/6), 243-252, doi:10.1023/a:1013123725860.

Seinfeld, J. H., and S. N. Pandis (2006), *Atmospheric Chemistry and Physics: From Air Pollution to Climate Change, 2nd Edition*.

Senff, C. J., R. J. Alvarez, II, R. M. Hardesty, R. M. Banta, and A. O. Langford (2010), Airborne lidar measurements of ozone flux downwind of Houston and Dallas, *J. Geophys. Res.*, *115*(D20), D20307.

Senff, C. J., J. Bösenberg, G. Peters, and T. Schaberl (1996), Remote Sensing of Turbulent Ozone Fluxes and the Ozone Budget in the Convective Boundary Layer with DIAL and Radar-RASS: A Case Study, *Beitr. Phys. Atmos.*, *69*(1), 161-176.

Shao, M., Y. Zhang, L. Zeng, X. Tang, J. Zhang, L. Zhong, and B. Wang (2009), Ground-level ozone in the Pearl River Delta and the roles of VOC and NOx in its production, *Journal of Environmental Management*, *90*(1), 512-518, doi:http://dx.doi.org/10.1016/j.jenvman.2007.12.008.

Sickles Ii, J. E., and D. S. Shadwick (2015), Air quality and atmospheric deposition in the eastern US: 20 years of change, *Atmos. Chem. Phys.*, *15*(1), 173-197, doi:10.5194/acp-15-173-2015.

So, K. L., and T. Wang (2003), On the local and regional influence on ground-level ozone concentrations in Hong Kong, *Environmental Pollution*, *123*(2), 307-317, doi:http://dx.doi.org/10.1016/S0269-7491(02)00370-6.

Solomon, P., E. Cowling, G. Hidy, and C. Furiness (2000), Comparison of scientific findings from major ozone field studies in North America and Europe, *Atmos. Environ.*, *34*(12-14), 1885-1920.

Stull, R. B. (1988), *An introduction to boundary layer meteorology*, Springer.

Sullivan, L. J., T. C. Moore, V. P. Aneja, W. P. Robarge, T. E. Pierce, C. Geron, and B. Gay (1996), Environmental variables controlling nitric oxide :emissions from agricultural soils in the southeast united states, *Atmos. Environ.*, *30*(21), 3573-3582, doi:10.1016/1352-2310(96)00086-6.

Tong, N. O., D. C. Leung, and C.-H. Liu (2011), A Review on Ozone Evolution and Its Relationship with Boundary Layer Characteristics in Urban Environments, *Water, Air, & Soil Pollution*, *214*(1-4), 13-36.

van Stratum, B. J. H., et al. (2012), Case study of the diurnal variability of chemically active species with respect to boundary layer dynamics during DOMINO, *Atmos. Chem. Phys.*, *12*(12), 5329-5341, doi:10.5194/acp-12-5329-2012.

Vilà-Guerau de Arellano, J., S. W. Kim, M. C. Barth, and E. G. Patton (2005), Transport and chemical transformations influenced by shallow cumulus over land, *Atmos. Chem. Phys.*, *5*(12), 3219-3231, doi:10.5194/acp-5-3219-2005.

Vilà-Guerau de Arellano, J., E. G. Patton, T. Karl, K. van den Dries, M. C. Barth, and J. J. Orlando (2011), The role of boundary layer dynamics on the diurnal evolution of isoprene and the hydroxyl radical over tropical forests, *J. Geophys. Res.*, *116*(D7), D07304, doi:10.1029/2010jd014857.

Vilà-Guerau de Arellano, J., K. van den Dries, and D. Pino (2009), On inferring isoprene emission surface flux from atmospheric boundary layer concentration measurements, *Atmos. Chem. Phys.*, *9*(11), 3629-3640, doi:10.5194/acp-9-3629-2009.

Wesely, M. L., and B. B. Hicks (2000), A review of the current status of knowledge on dry deposition, *Atmos. Environ.*, *34*(12–14), 2261-2282, doi:http://dx.doi.org/10.1016/S1352-2310(99)00467-7.

Wingo, S. M., and K. R. Knupp (2014), Multi-platform Observations Characterizing the Afternoon-to-Evening Transition of the Planetary Boundary Layer in Northern Alabama, USA, *Boundary-Layer Meteorology*, *155*(1), 29-53, doi:10.1007/s10546-014-9988-1.

Yegorova, E. A., D. J. Allen, C. P. Loughner, K. E. Pickering, and R. R. Dickerson (2011), Characterization of an eastern U.S. severe air pollution episode using WRF/Chem, *J. Geophys. Res.-Atmos.*, *116*(D17), D17306, doi:10.1029/2010JD015054.

Zhang, L., J. R. Brook, and R. Vet (2003), A revised parameterization for gaseous dry deposition in air-quality models, *Atmos. Chem. Phys.*, *3*(6), 2067-2082, doi:10.5194/acp-3-2067-2003.

Zhang, L., M. D. Moran, P. A. Makar, J. R. Brook, and S. Gong (2002), Modelling gaseous dry deposition in AURAMS: a unified regional air-quality modelling system, *Atmos. Environ.*, *36*(3), 537-560, doi:10.1016/s1352-2310(01)00447-2.

Zhang, Y., M. Bocquet, V. Mallet, C. Seigneur, and A. Baklanov (2012), Real-time air quality forecasting, part II: State of the science, current research needs, and future prospects, *Atmos. Environ.*, *60*(0), 656-676, doi:10.1016/j.atmosenv.2012.02.041.

Zoogman, P., et al. (2017), Tropospheric emissions: Monitoring of pollution (TEMPO), *Journal of Quantitative Spectroscopy and Radiative Transfer*, *186*, 17-39, doi:http://dx.doi.org/10.1016/j.jqsrt.2016.05.008.